Electronic Supplementary Material (ESI) for Nanoscale.

Supporting Information: Rapid nanoparticle self-assembly at elevated temperatures

Dominik Gerstner and Tobias Kraus*

INM – Leibniz Institute for New Materials gGmbH

E-mail: Tobias.Kraus@leibniz-inm.de

Experimental Setup

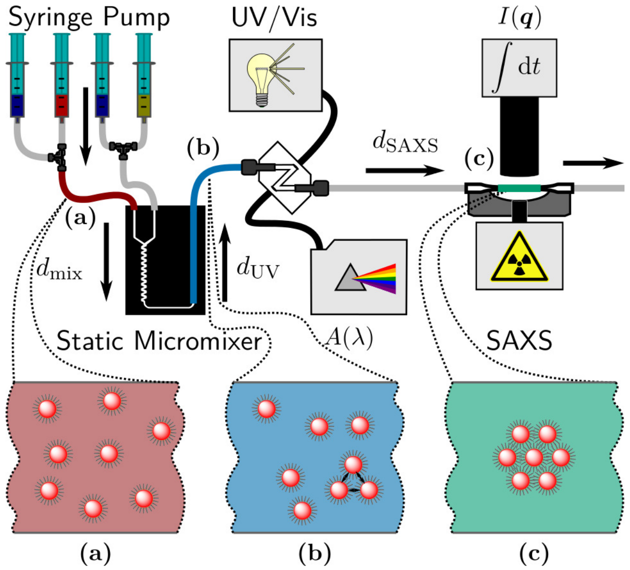

Figure 1: Schematic of the experimental setup. (a) A stable dispersion enters the mixing module. (b) After mixing with an incompatible solvent, attractive interparticle forces initiate agglomeration. (c) Steady states of agglomerate growth are observed.

The experimental setup is sketched in FIG. 1. The sample flow ($2.5\,\mu\mathrm{L\,s^{-1}}$ to $50\,\mu\mathrm{L\,s^{-1}}$) is driven by a pulsation-free syringe pump (“NEMESYS”, cetoni GmbH). Stable particle dispersions and incompatible solvents are blended in a static micromixer (‘MR-Lab MX”, Little Things Factory GmbH). The agglomerating sample is transported downstream and observed at fixed detector positions. Due to the steady-state flow conditions, the observed sample at the detectors corresponds to a steady-state of agglomeration. Connectors are made from PEEK and FEP, the detector cells and micromixer are glass parts.

The mixer, the UV/Vis cell and large parts of the tubing were immersed in a thermostated water bath to control the temperature. The SAXS capillary holder was thermostated with a bore hole in the metal part connected to the thermostat.

UV/Vis absorbance spectra were recorded with a custom-made, glass-capillary flow cell. A combined deuterium and halogen based lamp (Micropack "DH-2000-BAL") served as an intense white light source. An Ocean Optics "USB2000+" spectrometer detects the transmitted spectra with a grating and a linear CCD detector.

X-rays with an energy of 11 keV ($\lambda = 0.113\,\mathrm{nm}$) were selected from the synchrotron spectrum and collimated by a number of slits to form a parallel beam with dimensions of $450\,\mu\mathrm{m} \times 20\,\mu\mathrm{m}$. In a distance of $\sim 1.8\,\mathrm{m}$ to the sample position, the scattering signal was detected with an Aviex "PCCD170170" 2d CCD detector that has an active area of $171\,\mathrm{mm} \times 171\,\mathrm{mm}$ and was set to an effective pixel size of $166.8\,\mu\mathrm{m}$.

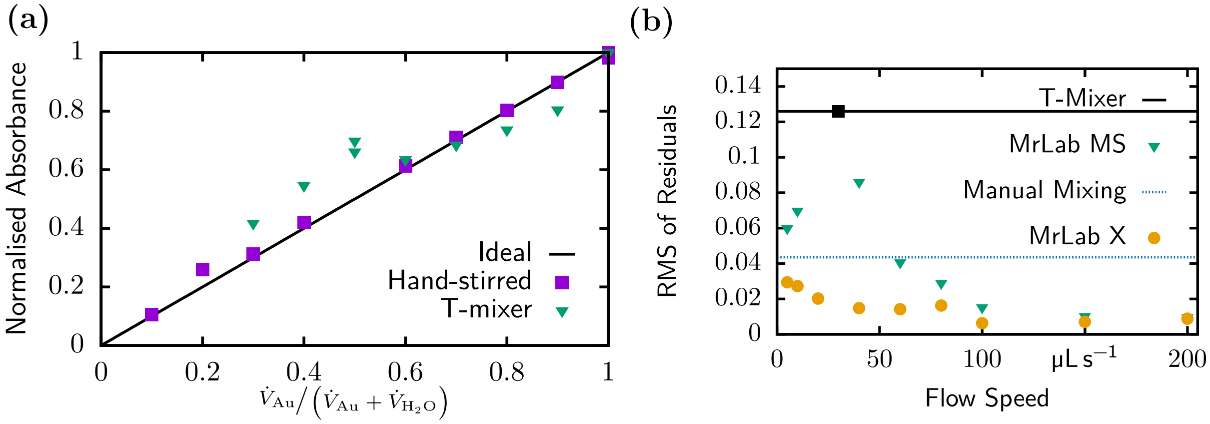

Figure 2: (a) Ideal mixing behavior compared to manual and online mixing with a T-piece. (b) The root mean square of residuals from a linear fit is a measure for the mixing efficiency of different methods.

To ensure sufficient mixing performance, we compared the mixing efficiency of the used

"MrLab X" mixing module with other mixing methods: Manual stirring, a simple T-piece and a different static micromixer ("MrLab MS"). Ideally, the magnitude of absorbance depends linearly on the concentration of the absorbing substance (Lambert-Beer law[1]). We associate non-linearities (as presented by the T-piece-mixed results in FIG. 2) with inhomogeneous mixing. To compare mixing performances, the root-mean-square-deviation of the measured normalized absorbances (corresponding to the points in FIG. 2 (a)) with respect to the linear behavior (corresponding to the line in FIG. 2 (a)) are compared between different mixing methods and at different velocities in FIG. 2 (b). The "MrLab X" module employed here outperforms all other methods in the complete flow velocity range and is therefore well-suited for our study.

Particle Synthesis

For a typical synthesis, 500 mg of dry chloroauric acid were dissolved under vigorous stirring in a mixture of 45 mL *n*-heptane and 45 mL oleylamine. After dissolution, 200 mg borane tert-butylamine complex (TBAB, $(CH_3)_3CNH_2{\cdot}BH_3$) dissolved in a mixture of 5 mL *n*-heptane and 5 mL oleylamine were added. The solution was stirred at room temperature for 1 h and the typical red color of a gold nanoparticle dispersion developed. To wash the dispersion from excess synthesis reagents, the AuNPs were precipitated by ethanol addition and centrifugation. After removing the supernatant, the precipitate was resuspended in 100 mL *n*-heptane.

Several 10 mL aliquots were taken to exchange the oleylamine on the surface with different alkylthiols (C12, C16) according to a procedure described in.[2] 472 mg triphenylphosphane and the corresponding thiol (364 mg C12, 465 mg C12) were dissolved in 10 mL *n*-heptane and the solution was heated to 90 °C. The dispersion aliquots were also heated and poured in the thiol solutions. After shaking gently, the solution was left undisturbed until it cooled down and the ligand exchange was completed. After cooling the excess reagents were removed by washing. The particles were precipitated by adding ethanol and centrifugation. After removing the supernatant, the precipitate was redispersed in 10 mL heptane. The product was a stable dispersion of gold nanoparticles, with core radii around 3.0 ± 0.2 nm (according to form factor fits of the SAXS data of a stable dispersion), stabilized with C12 or C18.

Calculation and Approximation of Structure Factors

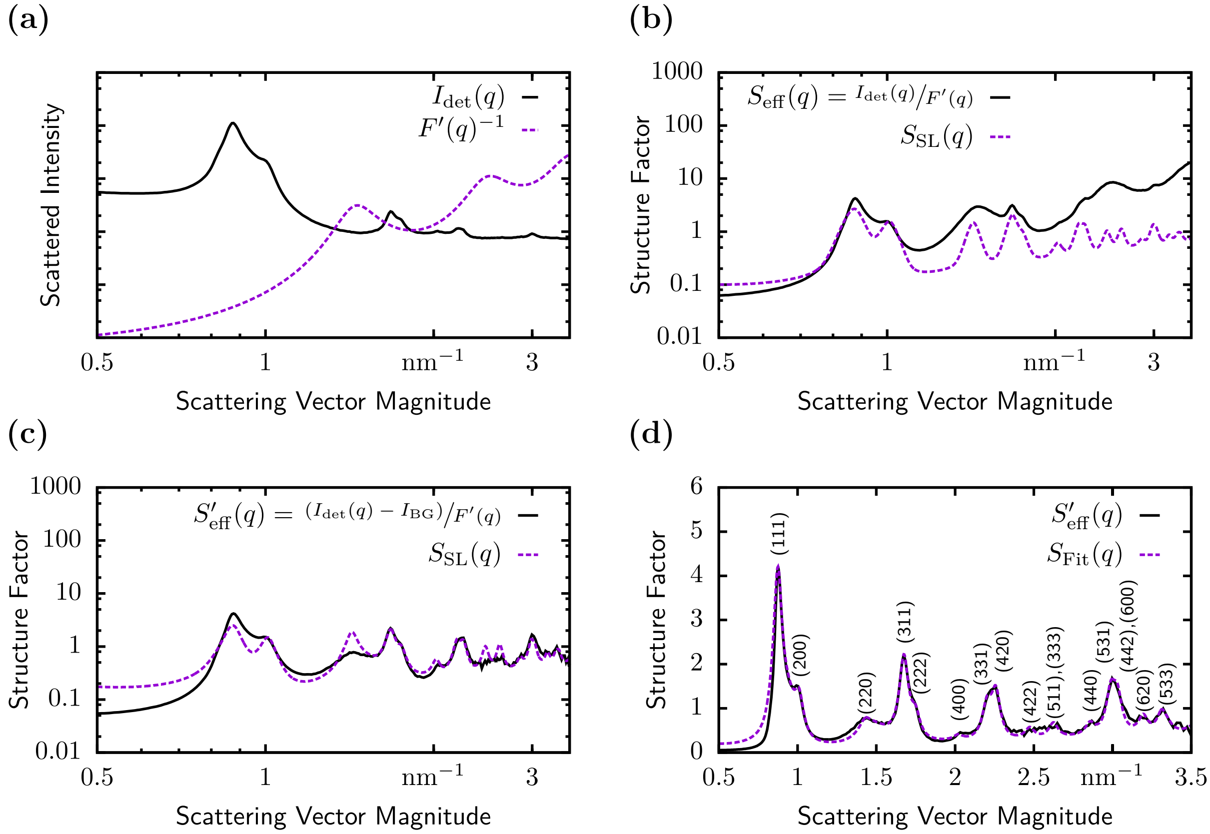

Figure 3: Illustration of the structure factor model construction. (a) I_{det} and $F'(q)^{-1}$ are multiplied to obtain S_{eff}. (b) S_{eff} deviates from the Förster model mainly at the form factor minima. (c) Subtracting a constant background from the scattered intensity improves the fit. (d) The full model function S_{Fit} captures the main features of the measured structure factor S'_{eff}.

According to the monodisperse approach, the scattering intensity $I(q)$ of superstructures of uniform particles with sufficient isotropy can be factorized[3] into a form factor $F(q)$, describing the scattering of non-interacting particles, and a structure factor $S(q)$, describing the scattering due to spatial correlations:

$$I(q) = F(q) \cdot S(q). \tag{1}$$

The form factor of particles with a certain dispersity $F'(q)$ can be expressed as an average of the size-dependant form factor weighted with the number distribution. Analytical solutions for the average are available for spherical particles with sizes following a Schulz-Zimm distribution.[3] The Schulz-Zimm distribution has a single peak with negligible tails and was used here to describe the size distribution of gold nanoparticles with radius R and standard deviation σ.

To analyze the agglomerate structure, the effective structure factor

$$S_{\text{eff}} = \frac{I_{\text{det}}(q)}{F'(q)} \tag{2}$$

was calculated from the background-corrected, scattered intensity of the agglomerates $I_{\text{det}}(q)$ and the particle form factor $F'(q)$, determined by fitting the scattered intensity of a stable dispersion with identical concentration.

The construction of S_{eff} can be visualized as the summation of $I_{\text{det}}(q)$ and $F'(q)^{-1}$ on a logarithmic scale. The curves in FIG. 3 (a) are added to obtain S_{eff}, the black line in FIG. 3 (b).

The structure factor of a given ordered, nanoparticle superlattice structure $S_{\text{SL}}(q)$ can be calculated based on the flexible model function from.[4] It combines a peak function (convolution of Gaussian and Lorentzian functions) with the known positions and relative intensities of a given lattice type and includes additional scattering due to size dispersity and lattice disorder. The calculated form factor $S_{\text{SL}}(q)$, based on estimated parameters, is compared to the measured S_{eff} in FIG. 3 (b). S_{eff} exceeds $S_{\text{SL}}(q)$ in a pattern that strongly resembles the inverse of the form factor $F'(q)$ (compare FIG. 3 (a)). This effect is found for all measurements.

The difference can be explained by assuming an additional, homogeneous signal that is detected concurrently to the actual agglomerate signal. We assume that the signal originates from a combination of noise at low signal strengths and a homogeneous scattering contribution from deposited material due to fouling of the SAXS capillary. We compensate this effect by subtracting a homogeneous intensity I_{BG} from the detected agglomeration signal $I_{\mathrm{det}}(q)$ prior to the division. I_{BG} is adjusted for every measurement to achieve a flat structure factor slope at large q. The resulting modified, effective structure factor $S'_{\mathrm{eff}} = {}^{(I_{\mathrm{det}}(q)\,-\,I_{\mathrm{BG}})}\!/_{F'(q)}$ agrees better with the model function $S_{\mathrm{SL}}(q)$ as presented in FIG. 3 (c).

While the peak positions (at intermediate and larger angles) corresponded to a fcc lattice for all ordered superlattices observed here, the observed relative peak heights could not be reproduced (as shown in FIG. 3 (c)). The largest deviations were found at the form factor minima positions (around $q \sim 1.5\,\mathrm{nm}^{-1}$ and $q \sim 2.5\,\mathrm{nm}^{-1}$, compare FIG. 3 (a)) and are likely caused by sensitivity variations of the detector due to the overall reduced intensity at these q values. To compensate the inhomogeneities and extract parameters from fitted structure factors anyway, Förster's model $S_{\mathrm{SL}}(q)$ was slightly modified to allow adjustment of the individual peak heights resulting in $S'_{\mathrm{SL}}(q)$.

Additional contributions were added to improve the model:

- To compensate the strong decrease of detector sensitivity in the primary minimum of the particle form factor, a single broad peak $P(q)$ at the position of the minimum was added.

- An additional peak $S_{\mathrm{A}}(q)$, attributed to disordered agglomerates, was added to the function at q values between the first two superlattice peaks.

- At small angles, the scattered intensity is dominated by the scattering caused by the contour of the agglomerates. It was described by adding the Debye-Büche function $S_{\mathrm{DB}}(q) \propto q^{-4}$[5] to the model.

The complete model used to approximate the effective form factor, termed "extended

Frster model" in the text, was

$$S_{\mathrm{Fit}}(q) = S'_{\mathrm{SL}}(q) + S_{\mathrm{DB}}(q) + S_{\mathrm{A}}(q) + P(q). \tag{3}$$

A fit of this complete model to the measured effective structure factor is compared to the experimental data and indexed with fcc reflections in FIG. 3 (d). With all the additions, the model approximates the data satisfactorily.

Calculation of Interaction Energies

Here, we estimate the interaction potentials between particles under different conditions. The objective is to test the Noro-Frenkel-theorem and provide a range of interaction potentials that allows for self-assembly rather than amorphous agglomeration of the attractive particles.

The interactions between nanoparticles with diameters below 10 nm and nanometer-thick ligand shells are dominated by their ligands.[6–9] The free energy of mixing for long polymers[10] has been used to model ligand-ligand interactions between particles with ligand monolayers such as the alkylthiols employed here.[11] Flory-Huggins theory is often used to describe nanoparticle behavior.[8,11,12] The interaction energy U_{mix} for overlapping ligand layers (at surface separations r larger than a single ligand length ℓ) of particles with radius R is written as

$$\frac{U_{\mathrm{mix}}(r)}{k_{\mathrm{B}}T} = \frac{\pi R}{V_{\mathrm{s}}}\phi_{\mathrm{av}}^2 \left(\frac{1}{2} - \chi\right) \cdot (r - 2\ell)^2 \,, \tag{4}$$

where $k_{\mathrm{B}}T$ is the thermal energy, V_{s} the volume of a solvent molecule and ϕ_{av} the volume fraction of the ligand molecules in the volume enclosing the surface.[11]

$$\chi = \frac{V_{\mathrm{s}}}{k_{\mathrm{B}}T}\left(\delta_{\mathrm{s}} - \delta_{\mathrm{m}}\right)^2 + 0.34 \tag{5}$$

is the so-called Flory parameter It describes the ligand-solvent interactions via the Hildebrand solubility parameters δ_s and δ_m of the solvent and ligands respectively. For dissimilar solubility parameters, $\chi > 1/2$, and the interaction between ligands is attractive.

For increased overlaps ($0 < r < \ell$), the Flory mixing energy is

$$\frac{U'_\mathrm{mix}(r)}{k_\mathrm{B}T} = \frac{6\pi R}{V_\mathrm{s}}\phi_\mathrm{av}^2 \ell^2 \left(\frac{1}{2} - \chi\right) \cdot \left(\ln\frac{\ell}{r} + \frac{4r - 3\ell}{6\ell}\right). \tag{6}$$

A ligand compressed below its linear extension exerts a strong repulsion, due to the loss of configurational entropy for the chains.[13] An analytical expression for the repulsion energy is

$$\frac{U_\mathrm{elastic}(r)}{k_\mathrm{B}T} = 2\pi\nu R\left(r\left(\ln\frac{r}{\ell} - 1\right) + \ell\right), \tag{7}$$

where ν is the number of ligand molecules per surface area.[11] ν is difficult to assess experimentally, based on[11] we assume a value of $\nu = 6.65 \times 10^{18}\,\mathrm{m}^{-2}$. We estimated the other parameters as $V_\mathrm{s} \sim 1.8 \times 10^{-28}\,\mathrm{m}^3$,[11] $k_\mathrm{B}T \sim 4 \times 10^{-21}\,\mathrm{J}$ and $\delta_\mathrm{m} \sim 1.6 \times 10^4\,\sqrt{\mathrm{Pa}}$ for C12 (assuming the sulphur does not contribute to the solubility).[14]

At separations larger than two ligand lengths, $r > 2\ell$, we assume there is no ligand-mediated interaction. Despite its fast decay at long ranges, the van der Waals attraction therefore dominates the interaction at “large” surface separations. For interacting spheres in close approach, the van der Waals interaction can be written as

$$U_\mathrm{vdW}(r) = -\frac{A}{6}\left(4\frac{R^2(r+R)}{r^2(r+4R)} + \ln\frac{r(r+4R)}{(2R+r)^2}\right), \tag{8}$$

where A is the Hamaker constant.[11] The reported values for gold vary .[16] We use $A = 75.5 k_\mathrm{B}T$[11] as an estimate.

Hildebrand parameters are strictly valid only for unpolar solvents,[17] but they qualitatively describe the solubility of polar solvent mixtures as we use them here. Solubility parameters δ_s for the different solvent compositions were estimated using a linear mixing rule for the Hildebrand parameters of 1-propanol ($\delta_\mathrm{prop} = 2.4 \times 10^4\,\sqrt{\mathrm{Pa}}$[18]) and heptane ($\delta_\mathrm{hep} = 1.5 \times 10^4\,\sqrt{\mathrm{Pa}}$[19]): $\delta_\mathrm{s} = \phi_\mathrm{prop} \cdot \delta_\mathrm{prop} + (1 - \phi_\mathrm{prop}) \cdot \delta_\mathrm{hep}$.

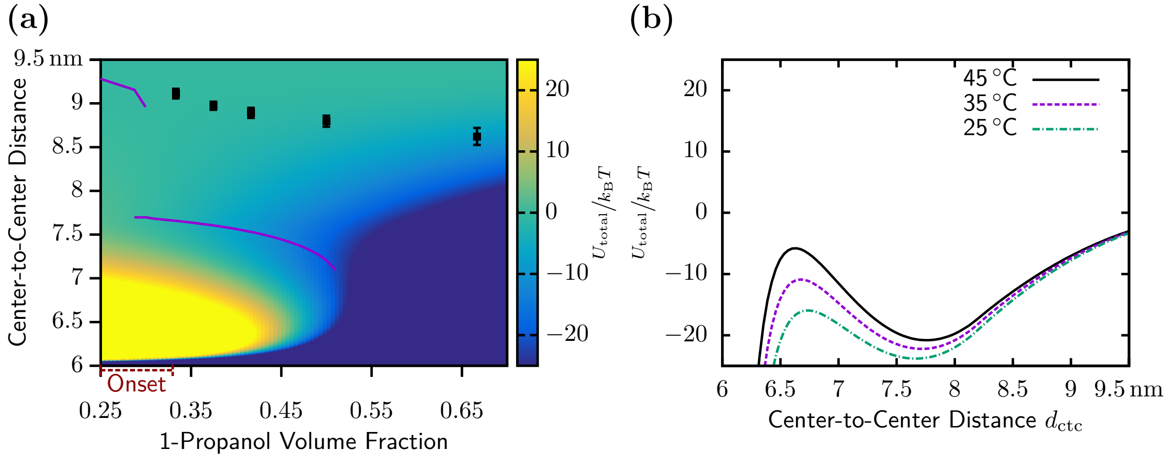

Figure 4: (a) Calculated interaction potential between 2 particles (color scale, cut-off at $\pm 25 k_\mathrm{B}T$) at different solvent compositions and distances at 35 °C. Experimentally determined next-neighbor distances are indicated by black dots. Local energy minima are marked with a solid purple line. The experimentally observed onset of agglomeration lies in the concentration range labeled with a dashed red line on the concentration axis. (b) Selected Energy-Distance profiles for C16-stabilized particles at $\phi_\mathrm{prop} = 0.2$.

The solvent-dependent energy landscape at $T = 35\,^\circ\mathrm{C}$ shown in Fig. 4 (a) combines ligand-ligand and ligand-solvent interactions, contributions of the elastic repulsion of compressed ligand layers $U_\mathrm{elastic}(r)$, and the van der Waals attraction of the cores $U_\mathrm{vdW}(r)$;[11] the full potential is $U_\mathrm{total}(r, f) = U_\mathrm{vdW}(r) + U_\mathrm{elastic}(r) + U_\mathrm{mix}(r, f)$. Local energy minima (purple lines) were determined numerically; they represent the expected equilibrium interparticle distance. At $\Phi \gtrsim 0.32$, the attractive minimum depth reaches $U_\mathrm{total} < -{}^{3}\!/\!_{2} k_\mathrm{B}T$, the average kinetic energy of a particle. We expect agglomeration when the depth of the minimum falls below that value.

The calculated profiles for C16-stabilized particles at different temperatures are visualized in Fig. 4 (b). The energy profiles change markedly less for a temperature change compared to solvent changes (see main text).

Ligand Length

To assess the correlation between critical ordering temperature and ligand length, separate agglomeration experiments with comparable AuNPs with 3 different ligand lengths, dodecanethiol (C12), hexadecanethiol (C16) and octadecanethiol (C18) were performed. The particles were synthesized following the protocol described in.[9] The structure factors display a clear trend: Longer ligands require higher temperatures to form supercrystals from the particles. In the polar solvent used to induce agglomeration, longer ligands should actually be more soluble. Solubility alone therefore does not explain the structure formation behavior. A ligand layer phase transition explains the critical crystallization temperature better.

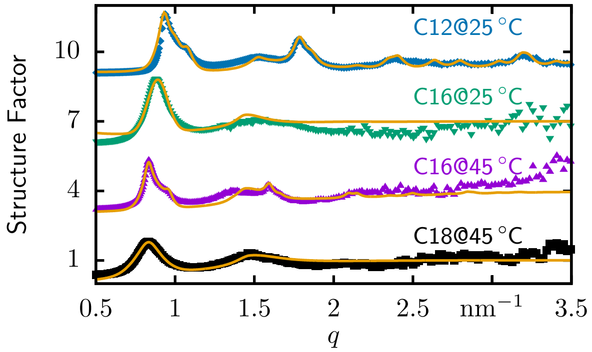

Figure 5: Structure factors of agglomerates grown at the indicated temperature with particles stabilized by the indicated thiol and the respective fits (offset by +3).

UV/Vis Absorbance Measurements

The UV/Vis absorbance spectra of steady states of agglomeration were measured with the same sample flow as the SAXS data presented in the paper. The UV/Vis detector was placed in line before the SAXS detector, the agglomeration time was therefore roughly half the age of the sample detected at the SAXS detector position. Relative comparisons are however possible.

UV/Vis spectroscopy is a standard tool for gold nanoparticle characterization and particularly sensible to their agglomeration. Dispersed gold particles exhibit a well-defined surface plasmon resonance peak around 516 nm. Coupling of the plasmons of contiguous particles induces a strong redshifted contribution in the absorbance spectra. Therefore the absorbance spectra are a sensible indication for agglomeration. Here, a custom-built transmission flow cell was coupled to a white light source and spectrometer via optical fibers. A combined deuterium and halogen lamp (Micropack "DH-2000-BAL") was used as a light source and the transmission spectra were detected with a grating-based CCD spectrometer (Ocean Optics "USB200+").

The UV/Vis results of the temperature-dependent measurements are summarized in FIG. 6 (a). The dispersed particles displayed the well-known surface plasmon resonance peak in the absorbance spectra. The spectra of agglomerates was characterized by an increased absorbance at higher wavelengths. For the amorphous agglomerates (according to the superlattice peaks), this lead to a broadened and red-shifted absorbance compared to the primary particles. For increasing long-range order, the absorbance displayed an increasingly separated red-shifted portion.

The emergence of red-shifted absorbance for agglomerates is usually attributed to new absorption modes appearing due to interparticle interaction of the localized plasmons.[20,21] The better separation for better superlattice quality likely results from two effects:

- Particles in superlattices are packed more closely compared to amorphous agglomerates. The interparticle plasmon is therefore more efficient in more ordered structures.
- The periodicity of a superlattices gives rise to additional resonances related to the structure.[22] These contributions would also increase for increased ordering.

The clear agglomerate absorbance in the spectrum at 25 °C justifies the assumption that the observed structure peak belongs to a static, glassy agglomerate and not to an increased interaction in a gas-like particle dispersion.

The UV/Vis results for the measurements at different 1-propanol contents in the 1-

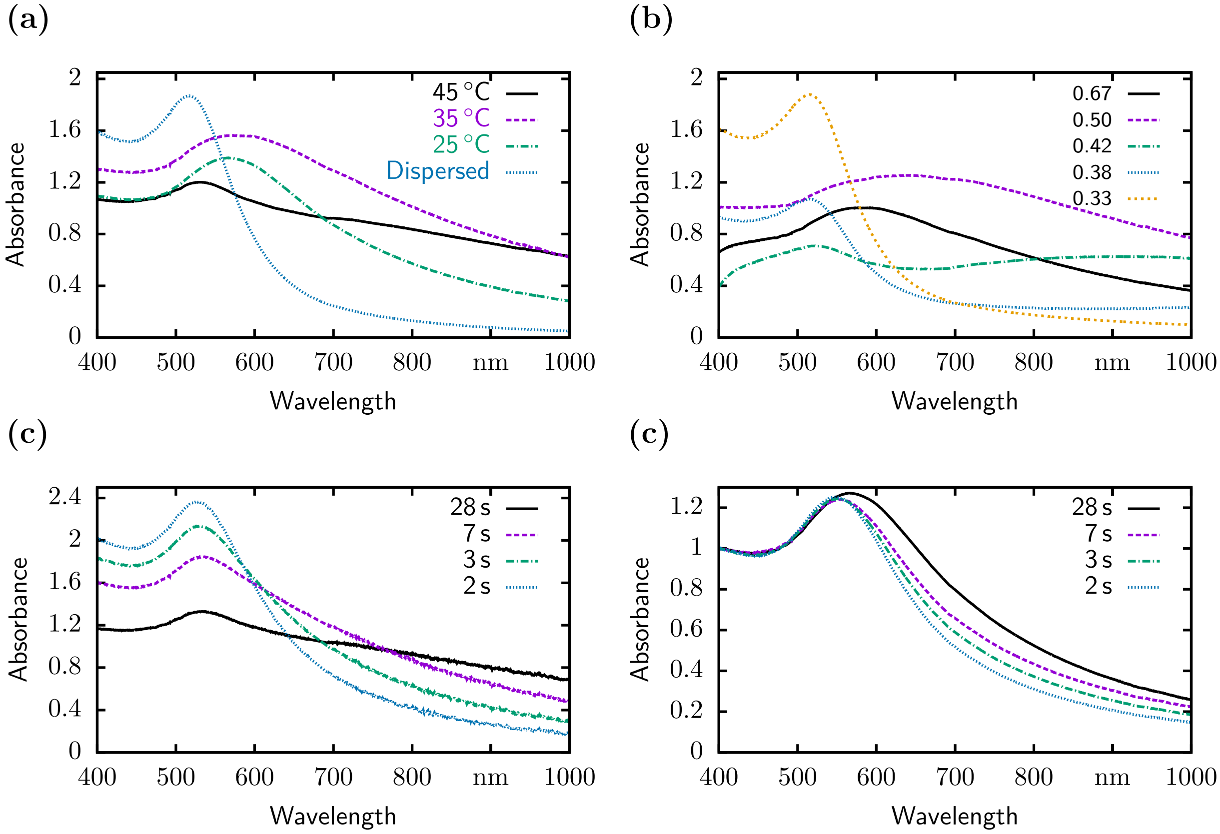

Figure 6: UV/Vis absorbance spectra of agglomerates corresponding to the SAXS patterns presented in the paper. (a) Agglomerates at different temperatures compared to the dispersed particles. (b) Agglomerates grown at different 1-propanol volume fractions. (c) Different stages of the agglomeration process at 45 °C. (d) Different stages of the agglomeration process at 25 °C.

propanol/n-heptane solvent are compiled in FIG. 6 (b). Similar to the temperature-dependant results in (a), the red-shifted parts (compared to the primary particle peak) increased for increasing superlattice quality. At higher 1-propanol contents ($\phi_{\text{prop}} = 0.67$ and $\phi_{\text{prop}} = 0.5$) the spectra appeared as a single, broad peak. The spectra at $\phi_{\text{prop}} = 0.42$ and $\phi_{\text{prop}} = 0.38$ displayed a clear red-shifted, second peak next to the primary particle plasmon peak. The spectrum at $\phi_{\text{prop}} = 0.33$ strongly resembled the primary particle spectrum.

The broadening and shift of the absorbance peak for the highest 1-propanol volume fractions was likely caused by superposition of the primary particle peak with a second, agglomerate-related plasmon peak. The agglomerate contribution is centered close to the primary particle peak because there is a considerable amount of amorphous agglomerates in the sample. The increased red-shift of the agglomerate absorbance for the intermediate 1-propanol fractions was likely caused by the increased portion of ordered superlattices compared to the highest 1-propanol fractions. Better packing and possible new resonances due to the lattice structure induce a larger red-shifted portion as explained above.

The agglomerate absorbance continuously shifted to higher wavelengths for different snapshots during the growth of agglomerates (FIG. 6 (c) and (d)). For the ordered superlattices (c) the arising absorbance was clearly separated from the primary particle peak. The amorphous agglomerates (d) displayed a broadening and shift of the primary particle peak for progressing agglomeration.

In summary, all UV/Vis results clearly demonstrate the influence of the particle arrangement on the optical properties of an agglomerate.

Velocity Influence

By tuning the total flow velocity at otherwise equal conditions, the growth times of the observed agglomerates are tuned.

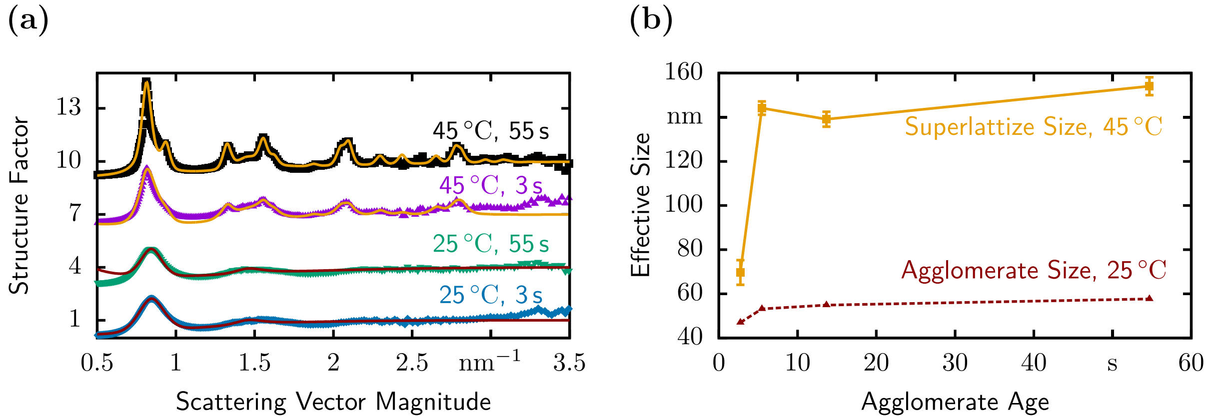

Figure 7: (a) Structure factors of agglomerates grown at the indicated temperature for the indicated time and the respective fits (offset by +3). (b) Ordered domain size (agglomerates grown at 45 °C) and effective agglomerate size (agglomerates grown at 25 °C) at different agglomeration stages.

The agglomeration of C16 stabilized particles was examined at 25 °C and 45 °C, therefore disordered and ordered agglomerates could be observed at the respective temperatures (see previous section). The total flow velocity was increased up to 100 µL s^{-1}, allowing to observe steady states of agglomeration with agglomerate ages below 3 s. The actual integration time was on the order of tens of seconds. The structure factors for the boundary values, at the earliest and latest agglomeration states, are compared in FIG. 7 (a). The high temperature measurements displayed the superlattice peaks introduced earlier. The main feature at low temperatures was a broad peak, related to amorphous agglomerates. The superstructure peaks narrowed for older agglomerates.

To further analyze the growth behavior, the superlattice domain sizes of the agglomerates grown at 45 °C is compared for different ages in the upper graph of FIG. 7 (b). Apart from the second point, the ordered domains grew continuously. Although the Scherrer equation (EQ. (1) in the main paper) is only defined for ordered superlattices, we calculated an effective agglomerate size from the position and width of the amorphous peak of the structure factors measured at 25 °C. This effective size (bottom graph in FIG. 7 (b)) grew continuously over the agglomeration time. Both growth curves were concave.

The growth behavior of ordered and disordered agglomerates was observed by scanning different steady states of agglomeration. The observation of agglomerates grown for 3 s over integration times of $\sim$ 10 s is enabled by our flow-based approach. The superlattice domain size rapidly grew in the first minute, similar to the effective size of the amorphous agglomerates. The initial growth was fast and slowed down at later stages. The curvature of the growth curves would favor a diffusion-limited agglomeration process (characterized by a power low growth curve) over a reaction-limited process (resulting in exponential growth).[23] However, the power law exponent corresponds to unphysically large fractal dimensions. This suggests a slowed down growth process compared to true diffusion-limited agglomeration. The slowing is likely caused by an additional barrier at close range due to the ligand layer. Due to the drastically reduced solubility of the ligand layer, the barrier effect is too small to result in truly reaction-limited agglomeration.

Notes and References

(1) Beer, A. *Annalen der Physik* **1852**, *162*, 78–88.

(2) Hiramatsu, H.; Osterloh, F. E. *Chemistry of Materials* **2004**, *16*, 2509–2511.

(3) Kotlarchyk, M.; Chen, S. *The Journal of Chemical Physics* **1983**, *79*, 2461–2469.

(4) Förster, S.; Timmann, A.; Konrad, M.; Schellbach, C.; Meyer, A.; Funari, S. S.; Mulvaney, P.; Knott, R. *The Journal of Physical Chemistry B* **2005**, *109*, 1347–1360.

(5) Pontoni, D.; Narayanan, T.; Petit, J.-M.; Grübel, G.; Beysens, D. *Physical Review Letters* **2003**, *90*, 188301.

(6) Talapin, D. V.; Shevchenko, E. V.; Kornowski, A.; Gaponik, N.; Haase, M.; Rogach, A. L.; Weller, H. *Advanced Materials* **2001**, *13*, 1868–1871.

(7) Eberle, A. P. R.; Wagner, N. J.; Akgun, B.; Satija, S. K. *Langmuir* **2010**, *26*, 3003–3007.

(8) Goubet, N.; Richardi, J.; Albouy, P.-A.; Pileni, M.-P. *Advanced Functional Materials* **2011**, *21*, 26932704.

(9) Geyer, T.; Born, P.; Kraus, T. *Physical Review Letters* **2012**, *109*, 128302.

(10) Evans, R.; Napper, D.-H. *Kolloid-Zeitschrift und Zeitschrift für Polymere* **1973**, *251*, 329–336.

(11) Khan, S. J.; Pierce, F.; Sorensen, C. M.; Chakrabarti, A. *Langmuir* **2009**, *25*, 13861–13868.

(12) Smitham, J. B.; Evans, R.; Napper, D. H. *J. Chem. Soc., Faraday Trans. 1* **1975**, *71*, 285–297.

(13) Evans, R.; Smitham, J. B.; Napper, D. H. *Colloid and Polymer Science* **1977**, *255*, 161–167.

(14) Brandrup, J.; Immergut, E. H.; Grulke, E. A.; Abe, A.; Bloch, D. R. *Polymer handbook*; Wiley New York, 1999; Vol. 89.

(15) Israelachvili, J. N. *Intermolecular and Surface Forces, Third Edition: Revised Third Edition*, 3rd ed.; Academic Press, 2011.

(16) Ref. 15, p. 266.

(17) Zeng, W.; Du, Y.; Xue, Y.; Frisch, H. L. In *Physical Properties of Polymers Handbook*; Mark, J. E., Ed.; Springer New York: New York, NY, 2007; pp 289–303.

(18) Lin, H.-M.; Nash, R. A. *Journal of Pharmaceutical Sciences* **1993**, *82*, 1018–1026.

(19) Barton, A. F. *CRC handbook of solubility parameters and other cohesion parameters*; CRC press, 1991.

(20) Ung, T.; Liz-Marzan, L. M.; Mulvaney, P. *The Journal of Physical Chemistry B* **2001**, *105*, 3441–3452.

(21) Hutter, E.; Fendler, J. *Advanced Materials* **2004**, *16*, 1685–1706.

(22) Ben, X.; Park, H. S. *The Journal of Physical Chemistry C* **2011**, *115*, 15915–15926.

(23) Lin, M. Y.; Lindsay, H. M.; Weitz, D. A.; Ball, R. C.; Klein, R.; Meakin, P. *Nature* **1989**, *339*, 360–362.